Textures of mantle peridotite rocks revisited

B. E. Tabor and H. Downes

Department of Earth and Planetary Sciences, Birkbeck University of London, Malet Street, London, WC1E 7HX, UK.

Abstract

In a continuing study of the textures of mantle peridotites, we have analysed thin-sections of additional samples including spinel and garnet peridotite xenoliths from a range of locations, using a grain-section skeleton outline method. Peridotites from ultramafic massifs have also been analysed using the same methodology. The results for all these samples lie on the same linear trend of grain-section area vs standard deviation as seen in our previous study. This confirms the utility of the quantitative method, providing observer-independent objective numerical descriptions of textures in peridotite rocks.

Two spinel peridotite xenoliths have been disaggregated using an Electric Discharge Disaggregation technique and sieved them to produce a grain size distribution. SEM imaging has been used to show that the 3D shapes of grains of the constituent minerals have concave features. CT-scanning of separated grains and rock cores has also demonstrated the concave features of the constituent minerals and their consequent interlocking structures.

A ‘perimeter-area’ relation technique has been used to show the 2-dimensional grain-section skeleton outlines clearly display fractal characteristics, authenticating our method by reference to established Euclidian and fractal patterns. The fractal nature of textures of mantle peridotite rocks is further supported by an alternative method for fractal assessment (Box Counting).

Keywords: textures, peridotite, fractal characteristics, Electric Discharge Disaggregation, CT-scanning

Introduction

It has long been recognised (e.g. Collee, 1963) that mantle peridotites show wide textural variations reflecting their history of deformation, recrystallization and grain growth. However textural nomenclature has varied greatly between different authors. The most widely used nomenclature for spinel peridotites is that of Mercier and Nicolas (1975). Harte (1977) reviewed and redefined textural terminology in general and included garnet peridotites, but other authors continued to add modifications and caveats to the basic classifications. Such qualitative criteria and assessments are inevitably subjective, as discussed by Swan and Sandilands (1995). To avoid this problem, features of an observed pattern should be defined and stated in terms of repeatable quantitative unambiguous measurements. Tabor (2005) and Tabor et al. (2010) developed a simple and effective definition method of texture of peridotites in thin-section which was applied by Tabor (2014) to a wide variety of peridotites.

For typical mantle peridotites, it is the grain size, shape and distribution that are most generally assessed in descriptions of texture. Humphries (1969) pointed out that if all the component particles in a rock were perfect spheres, there would be no problem of the definition of size or shape. A single dimension (e.g. diameter) would unequivocally specify both. However, the distribution of grain section-areas and shapes in thin-sections is a combination of the shape of the mineral, the size distribution of the mineral being sectioned, and a distribution produced by the random sectioning plane (Higgins, 1994; 2006). It is these features that are perceived as ‘texture’.

Most of the 43 samples studied by Tabor et al. (2010) were from the French Massif Central and the Eifel region in Germany, part of the Central European Volcanic Province (CEVP, Wilson & Downes, 1991) and therefore represented only a small region of the upper mantle. This present study was designed to test the conclusions of Tabor et al. (2010) on a wider range of peridotites and also to examine the contribution of crystal shape to the textural pattern seen in thin-section. We show that the mineral components of peridotite rocks have concave features that preclude any attempt at 3D visualisation from a single thin-section image (Howard & Reed, 1998) and that the textures of mantle peridotite rocks can best be described in terms of fractal parameters.

Methodology

Tabor et al. (2010) described a method of whole slide thin-section imaging that provides a skeletal image of the section. In a digitised form, the skeleton is analysed in terms of numbers and distributions of grain areas and outlines, and the statistics of their 2D distribution can be studied. From this data, Tabor et al. (2010) established a linear relationship between the size of the mean grain-section areas and the standard deviations of the grain-section area size for all mantle peridotite samples studied. This method provides a means for consistent comparison of samples that is independent of the observer.

There are clear variations in the shapes of the grain-section areas seen in peridotite thin-section, ranging from simple convex polygons to complex involute structures with re-entrant (concave) features. Clearly these must in some degree reflect the original three-dimensional structure of the original mineral grain being sectioned but the exact relationship is not obvious. To explore this further, two approaches have been used in this study: (1) disintegration of xenoliths by an electric discharge disaggregation (EDD) technique which leaves the original shape of the mineral grains intact and (2) *in situ* visualisation of mineral grain shapes by computer tomography (CT) scanning.

In order to explore the relation between the 3-dimensional mineral components of peridotites and their 2-dimensional textural images in thin-sections or on exposed surfaces, two spinel peridotite xenoliths (MR1, MR2) for which there was sufficient material available and for which thin-sections had already been prepared, were sent for EDD treatment at 'Selfrag' in Switzerland. EDD replaces the traditional compressive forces from crushing and grinding processes that can compromise the 'target' minerals, with an internally expansive tension causing the material to effectively explode along the mechanically weak mineral particle boundaries (Rudashevsky et al., 1995).

The resulting disaggregated material was divided by sieving into seven size fractions from > 2.0 mm to < 0.063 mm. Examination with a binocular microscope showed that most of the disaggregated grains were single mineral species. Amongst the coarsest fraction (>2.0 mm) however there were a small number that had not completely disaggregated and even in the next fraction (>1.0 mm) there were a few such grains. Computer-enhanced (image-stacking) optical examination of these grains confirmed their convoluted interlocking mineral components.

Examples of these grains were collected by hand from all but the smallest grain-size fraction and mounted on SEM stubs for detailed visualisation using a JEOL (JSM-6480LV) Scanning Electron Microscope at the Department of Earth Sciences, University College London. Mineral grains separated by EDD were also sorted into four groups: composite, olivine, orthopyroxene and clinopyroxene minerals. These were then mounted in cylinders cast from an acrylic polymer and scanned using an X-TEX Benchtop CT 160 X scanner at the University of Exeter. Initial experiments with a mantle xenolith fragment showed there was sufficient X-ray attenuation with some components for these to provide 3D image visualisation of their features. A rock fragment, however, has the disadvantage that the X-ray path length through the sample varies with orientation as the sample rotates in the X-ray beam. This can give rise to visual artefacts. The best solution is for the material being scanned to be presented in a cylindrical form rotating about the vertical axis, so cores were made of several large peridotite samples for CT-scanning.

Discrimination and visualisation of CT images depends on the X-ray attenuation of the components of the object being examined. With geological samples, the linear attenuation coefficients of the minerals are outside the control of the experiment so that the interpretation of overlapping peaks can be ambiguous. Although there are ‘seeding’ and ‘growth’ programs which address this issue in VGStudio MAX v 2.1 and in the literature (Ketcham, 2005), the display itself does not take account of the three-dimensional connectivity of comparable voxels, so that interpretation still to some extent depends on assumptions.

Developments in the visualisation and direct rendering of three-dimensional data on a two-dimensional display surface have been reviewed by Brodlie & Wood (2001). This involves the development of algorithms for the study of compositional variation in terms of connectivity, distribution and relative densities. This form of rendering, taking advantage of density gradients in a material, is more flexible than traditional indirect volume rendering in which a surface is used to delineate phase boundaries (Sakellariou et al. 2007). The computer program Drishti (Limaye, 2006), based on these principles, provides a facility to display the voxel density distribution either as simple cumulative 1D histograms or as 2D intensity gradients. The advantages of this approach are evident with CT results from the cylindrical cores of xenoliths examined in this study.

Analysed Samples

Using the methodology of scanning and skeletonising thin-sections described by Tabor et al. (2010), we have analysed additional spinel peridotite xenoliths from the French Massif Central (Hutchinson et al., 1975), Hungary (Downes et al., 1992) and Spain (Bianchini et al., 2010). We have also investigated spinel peridotite xenoliths from a Permian dyke at Streap Com'Laidh in Scotland (Upton et al., 2011), thus extending both the range of localities and ages of eruption of mantle xenoliths. Results are given in Tables 1 and 2 and shown on a plot of grain-section area vs standard deviation of area in Figure 1a.

Kimberlite-hosted spinel- and garnet-bearing peridotite xenoliths from the Udachnaya kimberlite pipe in Siberia (Boyd et al. 1997), and the De Beers mine, South Africa (Boyd et al. 1978), were also analysed and data reported in Table 3 and Figure 1b.

Ultramafic massifs also provide samples of mantle peridotites. Although their original textures may have been compromised by tectonic emplacement, many samples retain sufficiently undisrupted outlines of the original mineral grains to make possible a comparison with textural features in xenoliths. Sixteen thin-sections of a peridotite sample from Fontet Rouge (French Pyrenees, Fabries et al. (1991)) and a single thin-section from the nearby Lherz massif were examined, together with multiple thin-sections of a spinel peridotite from the Ronda massif (Betics, SE Spain; Frey et al. 1985), a harzburgite from Goro (Indonesia), and an almost monomineralic dunite from Mt. Dun (New Zealand, Coombs et al.1976). These measurements are reported in Table 4 and plotted in Figure 1c.

We have also explored the textural variations that are sometimes apparent within individual thin-sections such as DW83-20 (Fig. 2). The samples also included some that were of sufficient size to enable preparation of orthogonal thin-sections such as sample MR-1(i, ii, iii) (Table 1).

Results (1) Grain section areas

Data for the additional spinel peridotite xenoliths from Europe (Spain, France, Hungary and Scotland) are plotted in Figure 1a and are generally consistent with the trend line established by Tabor et al. (2010). For some of the xenoliths that could be sectioned in three orthogonal directions, the three resulting analyses yielded similar values and so clustered together about the trend line but for sample MR-1, the results spread out along the trend line to the extent that by qualitative assessment they would have been designated as different textures. This is also demonstrated by sample SZT 1068 (Downes et al. 1992), in which the plane of sectioning had provided a thin-section with two approximately equal halves (designated T and B in Table 2) of clearly different degrees of coarseness (Fig. 2). Nevertheless, the quantitative analyses are again still in accord with the established trend (Fig. 1a). In Table 2, the results shown for sample DW83-20* (a,b,c,d) are four approximately equal areas accounting for the whole thin-section that showed significant grain-section area size banding (Fig.2) which, if thin-sections normal to the current plane were prepared, might well be considered qualitatively differently.

Results for kimberlite-hosted peridotite xenoliths (Table 3) are again consistent with the previously observed trend (Fig. 1b), although the grain-section areas are much larger than for typical spinel peridotites. Results for samples from the ultramafic massifs (Table 4) also fall on the same trend as the xenoliths (Fig. 1c).

Results (2) SEM and CT scanning

After EDD and sieving, SEM imaging of the mono-mineralic grains in each size fraction showed a wide range of both simple and complex shapes, many of which had markedly concave surfaces (Fig. 3). Additionally, tri-lobate structures are present, suggesting the continuation of the mineral species through comparatively narrow, and relatively fragile, bridges into neighbouring volumes. The overview of sample MR2 (Fig. 3e) illustrates the wide range of shapes, from practically spherical to elongate irregular spindles, that are characteristic of all the sieved size fractions. Even in the smallest fraction that could be conveniently visualised, both concave surfaces and complex structures were evident.

Although the disaggregation and component visualisation by SEM tend to substantiate the non-convex nature of the mineral interfaces implied by their embayed outlines in thin-section, in situ visualisation better illustrates the extent and consequent influence on the perceived textures of the peridotite xenoliths. CT visualisation of separated mineral components from sample MR2 (Figs. 4 and 5A) largely confirms the SEM shapes. With the C-T individual images data files converted to the Drishti “Render”, the “Volume Exploration and Presentation Tool” was used to examine both the separated grains in the acrylic cast cylinders (e.g. Fig. 5A) and the *in situ* minerals in the xenolith rock cores themselves. With all the cast epoxy cylinders, the complex shapes of the separated grains were clearly displayed (e.g. Fig. 5A). For the rock core of xenolith RP83-68, the complex shapes of the in situ clinopyroxene minerals were clearly visible (Fig. 5B). At greater X-ray attenuations, a different form of mineral visualisation appears that is characteristic of the spinel components, consistent with spinel’s greater linear attenuation coefficient (Fig. 5C).

A similar situation is seen with the rock core of FR 1, from Fontet Rouge peridotite massif (Fig.5D). No spinel component however could be detected with this sample. This may well be an indication of the inhomogeneous distribution of this minor component or that it is of such a small size that its presence is lost in partial volume effects.

Thus, C-T scanning supports the view that the silicate mineral components in mantle peridotites are present in complex non-convex shapes and, for the clinopyroxenes, clearly demonstrates their involuted structures *in situ*. This is consistent with the images obtained in a study of spinel-pyroxene clusters (Bhanot et al. 2017). Where clearly visualised, the spinel shapes are in accord with their appearance in thin-sections.

Grain shapes in peridotite rocks

It is not only grain-section size variations but also their shapes that contribute to the assessment of what is generally described as ‘texture’ in thin-section. Although there are recognised terminologies for the qualitative description of particle shapes (Allen 1975), it is a difficult property to quantify or even define in a precise manner (Davis 1986). Orford & Whalley (1983) discussed the problem of quantifying irregular-shaped grain morphologies in sedimentology and Petford et al. (1993) similarly examined the digitised outlines of a serially sectioned feldspar grain from a granitoid. Both sets of workers concluded that fractal dimensions provided the best description of grain shapes especially where there were re-entrant features. For our work, a measure of the variation of two-dimensional shape has been quantified by comparing perimeter lengths of the grain-section outlines with their areas.

Textural patterns and the Characteristics of Fractals

Mandelbrot (1977) first recognised the importance and generality of the behaviour described by fractals in a wide range of natural forms and systems. The first key idea of fractal geometry is self-similarity, i.e. the object can be decomposed into smaller copies of itself (Hastings & Sugihara, 1993). Addison (1997) defined a fractal as an object “which appears self-similar under varying degrees of magnification”. The complexity is inherent, each small part replicating the structure of the whole. Turcotte (1997) made the point that scale invariance is a common phenomenon in Earth Science.

With natural fractals, Addison (1997) drew the distinction between statistical self-similarity (e.g. the ruggedness of a coastline) and exact self-similarity (e.g. the fronds of a fern being a mini-copy of the whole fern). With natural fractals there can be fundamental changes of the system limiting the range of the fractal description (e.g. the ruggedness of the coastline down to the roughness of the individual rocks and the component crystals). Meakin (1998) pointed out that it is rare for simple fractal models to provide an accurate description of nature over more than a few orders of magnitude. They nevertheless give a useful insight within their range of application.

The second characteristic idea of a fractal system is their dimensions. Unlike Euclidean dimensions which are integers, fractal dimensions are usually a non-integer between the topological and Euclidean dimensions. This can be seen from the work of Richardson (1961) on the relationship between the enclosed area (A) and its boundary perimeter (P). For regular Euclidean shapes (squares, circles, hexagons, triangles etc.), the ratio of the perimeter to the square root of the enclosed area is a constant ($R = P/\sqrt{A}$), regardless of the size of the shape (where R is a dimensionless ‘shape factor’) (Fig. 6).

This relationship can be generalised for areas bounded by fractal curves as:

$$\mathbf{R}_\delta = \mathbf{P}^{\,1/\mathbf{D}\delta}/\sqrt{\mathbf{A}}$$

where **P** and **A** are now the measured perimeter and the enclosed area, using a length scale δ, small enough to accurately measure the smallest of the boundaries and $\mathbf{R}_\delta$ is the shape factor determined by this method. From this it follows that $\mathbf{logA = 2/D_\delta\ logP - 2logR_\delta}$. This is the equation of a straight line with a slope of $\mathbf{2/D_\delta}$ and an intercept of $\mathbf{- 2\ log\ R_\delta}$, from which the fractal dimension ($\mathbf{D}_\delta$) and the shape factor ($\mathbf{R}_\delta$) can be deduced.

This method has been extensively used to characterise data sets (Addison, 1997; Agterberg & Cheng, 1999). In order to examine the applicability of this method to the present work, a number of test patterns were prepared, skeletonised and analysed. When the perimeter–area method was applied to Euclidean shapes, it returned the correct values of the shape factor and dimension, but it was necessary to explore the response of established fractal systems. Wegner et al. (1993) provided routines to generate and print many fractal types, of which 'barnsleyj2', formed of slightly distorted triangular units, is a reasonable formalisation of patterns seen in peridotite thin-sections (Fig. 7A).

The digitised skeletal image of 'barnsleyj2' (Fig. 7B) was then analysed, with an arbitrary scale, to give area, perimeter and longest axis values for each of the 1813 individual shapes making up the image. These values were then plotted on a log (A) vs log (P) graph (Fig. 8A) to give the trend line from which the fractal dimension ($\mathbf{D}_\delta$) and shape factor ($\mathbf{R}_\delta$) could be calculated. The same approach was applied to, and can be compared with, the skeleton of a thin-section of a spinel peridotite xenolith (Fig. 8B, Table 5).

Image analysis data, both from the examples listed by Tabor et al. (2010) and the present work (Tables 1 – 4), show log A/log P relationship plots with a major component clustering, with varying degrees of precision, around a trend line that can be interpreted to give fractal dimensions and shape factors. These values, although possibly influenced by the number of grain-section areas available for measurement in the samples being examined, all fall within a range indicative of fractal characteristics (Table 5).

Higgins (1994) clearly demonstrated the fundamental problem with interpreting thin-section images. He showed a series of two-dimensional images of the intersections of random planes with geometric solids such as cubes, prisms and tablets of various dimension ratios. Three of these published images were converted to skeletons (Fig. 9), digitised and analysed, with the same calibration value, to give log area vs. log perimeter graphs for the three separate images (Fig. 10). The resulting trend lines provided the corresponding fractal dimensions' (**D**$_\delta$) and shape factors (**R**$_\delta$**)** in Table 5.

Comparison of the measured values in Table 5 with those for basic Euclidean shapes (Fig. 6) shows that the perimeter - area relationship responds as expected to the change to fractal geometries. Even the cube section shapes begin to diverge from Euclidian geometry in the second decimal place (Table 5). Those for the prism and tablet sections show clear fractal characteristics so that Higgins' (1994) work raises the question of the extent to which the perceived pattern on a surface or in a thin-section is the product of the sectioning process or the underlying mineral distribution.

Fractals and Power Law Scaling

The third important characteristic of fractal systems is the power law relationships that are central to their scale invariant symmetry and their progression from simple to complex behaviour. Meakin (1998) pointed out the need for adequate data to establish such functions but that many empirical equations in general use are of this form, e.g. the Rosin - Rammler equation (Kittleman 1964) which is widely used in industry (Bye 1999). Similarly, the log hyperbolic distribution introduced by Bagnold and Barndorff-Nielsen (1980) fulfils this requirement and is not incompatible with the present study. Armienti and Tarquini (2002) also proposed a power law distribution to account for the size distribution of olivine crystals in mantle xenoliths.

Fractals can be defined as geometric objects which exhibit scale-invariance, leading to a class of scaling rules, ‘power laws’ characterized by scaling exponents. One of these exponents is the subject of the perimeter-area relationship described above and reviewed by Cheng (1995). With Euclidean shapes, the ratio of the perimeter to the square root of the enclosed area is a constant regardless of the size of the shapes (Addison 1997) and with a scaling exponent of effectively unity but which is exceeded by a non-integer dimension for a fractal set. Another important means of classifying fractals is the Hausdorff (1919) dimension exponent which Mandelbrot (1982) proposed as the definition of a fractal when this exceeded the topological dimension. The complexity of the mathematics for the Hausdorff dimension makes this difficult to calculate for real data and so the closely related ‘box counting’ dimension finds frequent application in a range of practical situations (Addison 1997). The ‘box counting’ dimension is particularly suitable for computer realization, by applying rectangular grids of different grid side lengths to a two dimensional pattern, and counting the number of the consequent boxes that contains part of the fractal outline. The variation of this number with increasingly smaller boxes provides an estimate of the fractal dimension and its variation over the range of measurement.

A convenient program for box counting is available for MatLab (Moisy, 2008). The actual ‘box count’ is compared with that which would result from a simple space filling count of boxes that would be expected to follow a power law relation with an exponent of two. The divergence of the two counts is an indication of the fractal characteristic of the pattern. This is further demonstrated by a plot (local dimension) of the rate of change of the count with decreasing box size. The method was applied to an established fractal pattern, barnsleyj2 (Barnsley et al. 1986; 1988) which had been used previously to establish the perimeter-area relationship (Figs. 8A and 8B). The box counting method was then applied to examples of peridotite skeleton outlines (Figs. 11a, 11b) and confirmed the fractal characteristics of the peridotite textures.

Conclusions

The inclusion of a further 100 samples confirms that the method of whole slide scanning and thin-section skeleton images analysis established by Tabor et al. (2010) provides a robust quantitative, observer-independent description for mantle peridotites from a wide range of origins. Some rocks show textural variations which vary in their grain-size and hence plot in different places along the established trend line. Using EDD, SEM and CT scanning techniques, the shapes of individual grains in the peridotites have been shown to be complex and non-convex. Application of a perimeter-area technique to samples both from the previous study and the current study, together with box counting, demonstrates that grain shapes in peridotites show fractal characteristics.

Acknowledgements

We acknowledge the following colleagues for donating samples to our work: Pamela Kempton (Streap), Nikolai Vladykin (Siberia), Csaba Szabo (Hungary), Emma Humphreys-Williamson (Spain), Birkbeck Departmental collection. We also acknowledge the use of the CT scanner and help of the staff at the University of Exeter. We thank Selfrag (Switzerland) for their help in disaggregating two xenoliths. Thanks to Jim Davy (UCL) for assistance with the

SEM. This research did not receive any specific grant from funding agencies in the public, commercial, or not-for-profit sectors.

References

Addison, P. S. 1997. Fractals and Chaos: an illustrated course. Institute of Physics Publishing, Bristol. (Reprinted with minor corrections 2001).

Agterberg, F. P. & Cheng, Q. 1999. Guest Editorial; Introduction to Special Issue on “Fractals and Multifractals”. Computers & Geosciences, 25, 947-948.

Allen, T. 1975. Particle Size Measurement, Second Edition. Chapman and Hall, London.

Armienti, P. & Tarquini, S. 2002. Power law olivine crystal size distributions in lithospheric mantle xenoliths. Lithos 65, 273-285.

Bagnold, R. A. & Barndorff-Nielsen, O. 1980. The pattern of natural size distributions. Sedimentology, 27, 199-207.

Barnsley, M. F., Ervin, V., Hardin, D. & Lancaster, J. 1986. Solution of an inverse problem for fractals and other sets. Proceedings of National Academy of Sciences USA, 83, 1975-7.

Barnsley, M. F. 1988. Fractals everywhere. Academic Press, Boston.

Bhanot, K. K. Downes, H. Petrone, C. M. & Humphreys-Williamson, H. 2017. Textures in spinel peridotite mantle xenoliths using micro-CT scanning: Examples from Canary Islands and France. Lithos, 276, 90-102.

Bianchini, G., Beccaluva, I., Bonadiman, C., Nowell., G. M. Pearson, D. G., Siena, F. & Wilson, M. (2010). Mantle metasomatism by melts of HIMU piclogite components: new insights from Fe-lherzolite xenoliths (Calatrava Volcanic District, central Spain). In: Petrological Evolution of the European Lithospheric Mantle, Geological Society London, Special Publications, 337, 107-124.

Boyd, F. R., Pokhilenko, N. P., Pearson, D. G., Mertzman, S. A., Sobolev, N. V. & Finger, L. W. 1997. Composition of the Siberian cratonic mantle: evidence from Udachnaya peridotite xenoliths. Contributions to Mineralogy and Petrology, 128, 228-246.

Boyd, F. R. & Nixon, P. H. 1978. Ultramafic nodules from the Kimberlite pipes, South Africa. Geochimica et Cosmochimica Acta, 42, 1367-1382.

Brodlie, K. & Wood, J. 2001. Recent Advances in Volume Visualization. Computer Graphics Forum, 20, (2), 125-148.

Bye, G. C. 1999. Portland Cement, 2^{nd} Edition. Thomas Telford, London. Pp. 76-8.

Cheng, Q. 1995. The Perimeter-Area Fractal Model and its Application to Geology. Mathematical Geology, 27, (1), 69-82.

Collee, A. L. G. 1963. A fabric study of lherzolites with special reference to ultrabasic nodular inclusions in the lavas of Auvergne (France). Leidse Geologische Mededelingen, 28, 1-102.

Coombs, D. S., Landis, C. A., Norris, R.J., Sinton, J. M., Borns, D.J., Craw, D. 1976. The Dun Mountain ophiolite belt, New Zealand, its tectonic setting, constitution and origin, with special reference to the southern portion. American Journal of Science, 276, 561-603.

Davis, J. C. 1986. Statistics and Data Analysis in Geology, 2^{nd}. Edition. John Wiley & Sons, New York.

Downes, H., Embey-Isztin, A. & Thirlwall, M. F. 1992. Petrology and geochemistry of spinel xenoliths from the western Pannonian Basin (Hungary): evidence for an association between enrichment and texture in the upper mantle. Contributions to Mineralogy and Petrology, 109, 340-354.

Fabries, J., Lorand, J.-P., Bodinier, J.-L. & Dupuy, C. 1991. Evolution of the Upper Mantle beneath the Pyrenees: Evidence from Orogenic Spinel Lherzolite massifs. Journal of Petrology, Special Lherzolites Issue, 55-76.

Frey, F. A., Suen, C. J. & Stockman, H.W. 1985. The Ronda high temperature peridotite: Geochemistry and petrogenesis. Geochimica et Cosmochimica Acta, 49, 2469-2491.

Harte, B. 1977. Rock nomenclature with particular relation to deformation and recrystallisation textures in olivine-bearing xenoliths. Journal of Geology, 85, 279-288.

Hastings, H. M. & Sugihara, G. 1993. Fractals - A User's Guide for the Natural Sciences. Oxford University Press, Oxford.

Hausdorff, F. 1919. Dimension und ausseres Mass. Mathematisches Annalen 79,157-79.

Higgins, M. D. 1994. Determination of crystal morphology and size from bulk measurements on thin sections: numerical modelling. American Mineralogist, 79, 113-19.

Higgins, M. D. 2006. Quantitative Textural Measurements in Igneous and Metamorphic Petrology, Cambridge University Press, Cambridge.

Humphries, D. W. 1969. Mensuration methods in optical microscopy. *In:* Barer, R. & Cosslett, V. E. (eds) Advances in Optical and Electron Microscopy, Volume 3. Academic Press, London, 33 - 99.

Hutchison, R., Chambers, A. L., Paul, D. K. & Harris, P. G. 1975. Chemical variations from French ultramafic xenoliths; evidence for a heterogeneous upper mantle. Mineralogical Magazine, 40, 151-170.

Howard, C. V. & Reed, M.G. 1998. Unbiased Stereology, BIOS Scientific Publishers.

Ketcham, R. A. 2005. Computational methods for qualitative analysis of three-dimensional features in geological specimens. Geosphere, 1, 32-41.

Kittleman, L. R. 1964. Application of Rosin's Distribution in Size-Frequency Analysis of Clastic Rocks. Journal of Sedimentary Petrology 34(3), 483-502.

Limaye, A. 2006. Drishti – Volume Exploration and Presentation Tool. *Poster Presentation.* Vis 2006, Baltimore.

Mandelbrot, B. B. 1977. Fractals: Form, chance and dimensions. Freeman, San Francisco. English translation of Mandelbrot (1975), Les objects fractals: forme, hasard et dimension. Flammarion, Paris.

Mandelbrot, B. 1982. The Fractal Geometry of Nature, W. H. Freeman San Francisco.

Meakin, P. 1998. Fractals, scaling and growth far from equilibrium. Cambridge University Press, Cambridge.

Mercier, J-C. C. & Nicolas, 1975. Textures and fabrics of upper-mantle peridotites as illustrated by xenoliths from basalts. Journal of Petrology, 16, 454-487.

Moisy, F. 2008. Computing a fractal dimension with Matlab: 1D, 2D and 3D Box-counting. http://www.mathworks.co.uk/mathlabcentral/fileexchange/13063-boxcount/

Orford, J. D. & Whalley, W. B. 1983. The use of the fractal dimension to quantify the morphology of irregular- shaped particles. Sedimentology, 30, 655-668.

Petford, N., Bryon, D., Atherton, M. P. & Hunter, R. H. 1993. Fractal analysis in granitoid petrology: a means of quantifying irregular grain morphologies. European Journal of Mineralogy, 5, (3) 593-598.

Richardson, L. F. 1961. The problem of contiguity: An appendix of statistics of deadly quarrels. General Systems Yearbook, 6. 139-87.

Rudashevsky, N. S., Burakov, B. E., Lupal, S. D., Thalhammer, O. A. R. & Sani-Eidukat, B. 1995. Liberation of accessory minerals from various rock types by electric-pulse disintegration - method and application. Transactions of the Institute of Mining and Metallurgy. (Section C: Mineral Processing, Extraction and Metallurgy), 104, C25-C29.

Sakellariou, A. Arns, C. H. Sheppard, A. P. Sok, R. M. Averdunk, H. Limaye, A. Jones, A. C. Sendon, T. J. & Knackstedt, M. A. 2007. Developing a virtual materials laboratory. Materials Today, 10, (12), 44-51.

Swan, A. R. H. & Sandilands, M. 1995. Introduction to Geological Data Analysis. Blackwell Science, Oxford.

Tabor, F. A. 2005. Spinel lherzolite xenoliths, quantitative characterization of textures (Abstract). Ofioliti, 30(2), 221.

Tabor, F. A., Tabor, B. E. & Downes, H. 2010. Quantitative characterization of textures in mantle spinel peridotite xenoliths. In: Petrological Evolution of the European Lithospheric Mantle. Geological Society London, Special Publications, 337, 195-211.

Tabor, B. E. 2014. Quantitative petrology: the textures of peridotite rocks of sub-continental mantle origin. PhD Thesis, University of London.

Turcotte, D. L. 1997. Fractals and Chaos in Geology and Geophysics, 2nd. Edition. Cambridge University Press, Cambridge.

Upton, B. G. J., Downes, H., Kirstein, L. A., Bonadiman, C., Hill, P. G. & Natflos, T. 2011. The lithospheric mantle and lower crust-mantle relationships under Scotland: a xenolith perspective. Journal of the Geological Society of London, 168, 873-885.

Wegner, T., Peterson, M., Tyler, A. & Branderhorst, P. 1993. Fractals for Windows. Waite Group Press. California.

Wilson, M. & Downes, H. 1991. Tertiary-Quaternary extension-related alkaline magmatism in western and central Europe. Journal of Petrology, 31, 811-850.

Figure Captions

Fig. 1.a. Standard deviation versus mean grain-size for xenoliths collected from Neogene volcanic central Spain {Calatrava}, the French Massif Central {FMC}, the Central European Volcanic Province {CEVP} and the Pannonian Basin of Hungary {HPB}. The 'Streap' collection is from the Permian of Scotland. 'Trend' is the correlation found by Tabor et al. (2010). Data from Tables 1 and 2. b. Standard deviation versus mean grain-size for kimberlite-hosted xenoliths. Note the larger scale required for these coarser examples with the correspondingly smaller number of grain-section areas available for measurement in a standard thin-section which may influence the precision and account for the greater scatter observed whilst still being in general agreement with the previous 'Trend' line. Data from Table 3. c. Standard deviation versus mean grain-size for tectonically emplaced peridotites from the Pyrenees, Ronda, Goro and Mt Dun. Trend line as Tabor et al. (2010), Data from Table 4.

Fig. 2. Examples of thin-sections skeletons of spinel peridotite xenoliths showing apparent grain size banding: a, D8 Eifel (CEVP); b, DW83-20 Eifel (CEVP); c, SZT-1068 Hungary

Fig. 3. SEM images of examples of EDD grains from spinel peridotite mantle xenolith MR2.

Fig. 4. CT scan of EDD-released olivine grains from xenolith MR2 mounted in acrylic polymer cast cylinder.

Fig.5. A. Drishti ‘Render’ visualisation of EDD-separated grains from xenolith MR2 cast cylinder. B. Mineral visualisation at attenuation in situ, at X-ray attenuations attributed to the clinopyroxene component of the RP83-68 rock core. C. Mineral visualisation at greater attenuation densities, attributed to the spinel component of the RP83-68 rock core. D. Mineral visualisation at slightly greater attenuation densities, attributed to the clinopyroxene component of the FR 1 rock core.

Fig. 6. Perimeter-Area shape factors (R) derived for Euclidean figures where **L** is the side length or **D** the diameter as measures of the size; Square, R = 4; Circle, R = 3.5449; Hexagon, R = 3.7224; Triangle R = 4.5590.

Fig. 7. A. Fractal pattern generated by ‘Winfract’ (Wegner et al. 1993) for ‘barnsleyj2’. B. Skeletal image drawn from A.

Fig. 8.a. Perimeter - Area relationship for ‘Fractal barnsleyj2 (Fig. 6B). b. Perimeter - Area relationship for spinel peridotite xenolith RP91-7 (1356 grain-section areas).

Fig. 9. Test images prepared from random sections of regular solids (Higgins, 1994). A. a cube (1:1:1). B. a prism (1:1:10). C. a tablet (1:10:10)

Fig. 10. Perimeter area relationships for the separate test images Fig. 9A; Fig. 9B; Fig. 9C, yielding different values for ($\mathbf{D}_{\delta}$) and ($\mathbf{R}_{\delta}$), Table 5.

Fig. 11. a. The barnsleyj2 fractal pattern (top panel) is similar to a mineral skeletal outline and on the Log-Log Plot (middle panel) shows a clear divergence from the space filling box-count consistent with its known fractal characteristics. This is further supported by the differential (local dimension) curve (bottom panel). b. Bt 25 a fine-grained spinel peridotite xenolith from the French Massif Central showing a very similar pattern of behaviour to that of the barn2s fractal pattern. Top panel = skeletal outline; middle panel = log-log plot; bottom panel = box counting.

Figure

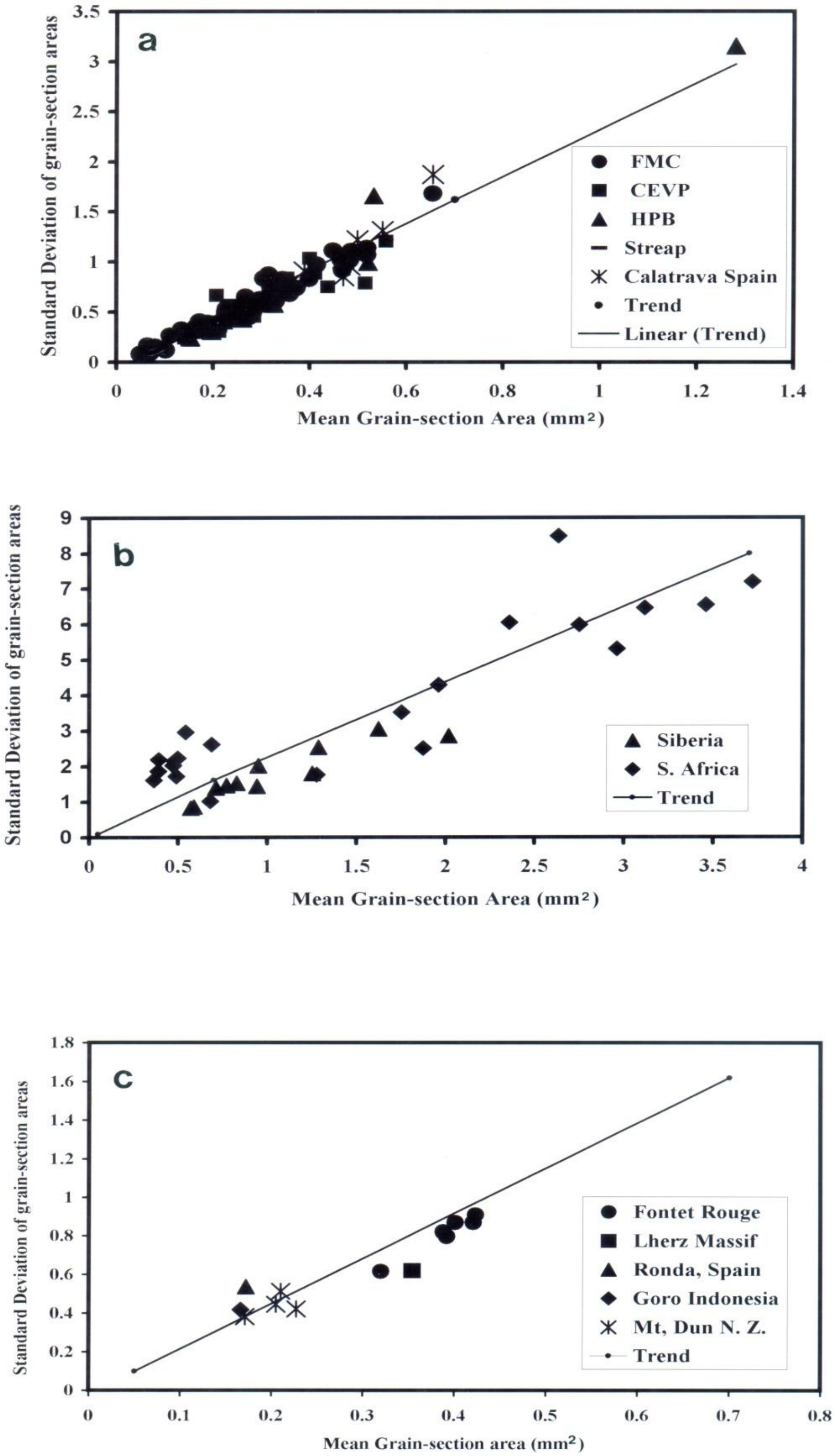
a
Standard Deviation of grain-section areas
Mean Grain-section Area (mm²)
FMC
CEVP
HPB
Streap
Calatrava Spain
Trend
Linear (Trend)
b
Standard Deviation of grain-section areas
Mean Grain-section Area (mm²)
Siberia
S. Africa
Trend
c
Standard Deviation of grain-section areas
Mean Grain-section area (mm²)
Fontet Rouge
Lherz Massif
Ronda, Spain
Goro Indonesia
Mt, Dun N. Z.
Trend

Figure

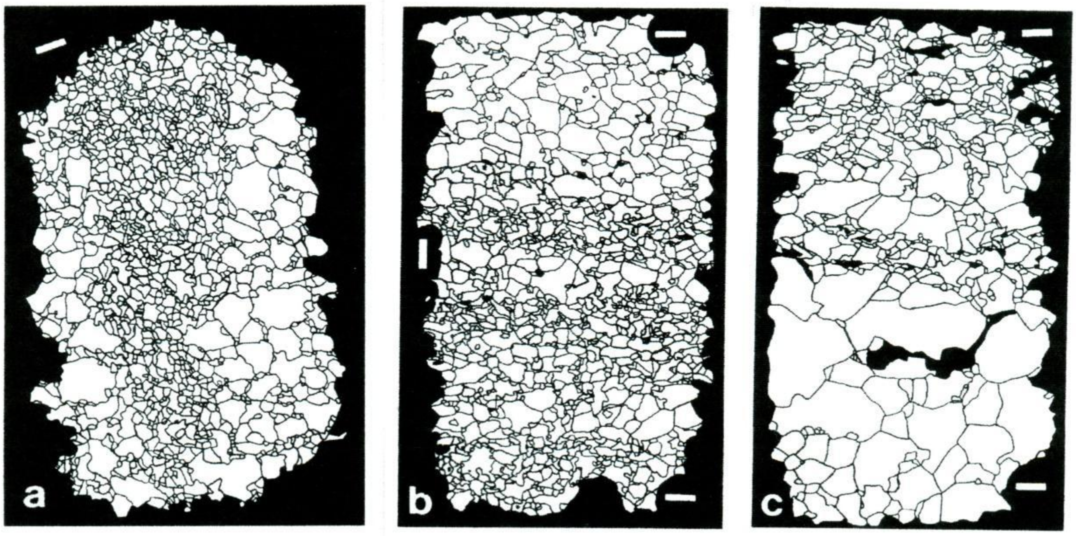

Figure 3

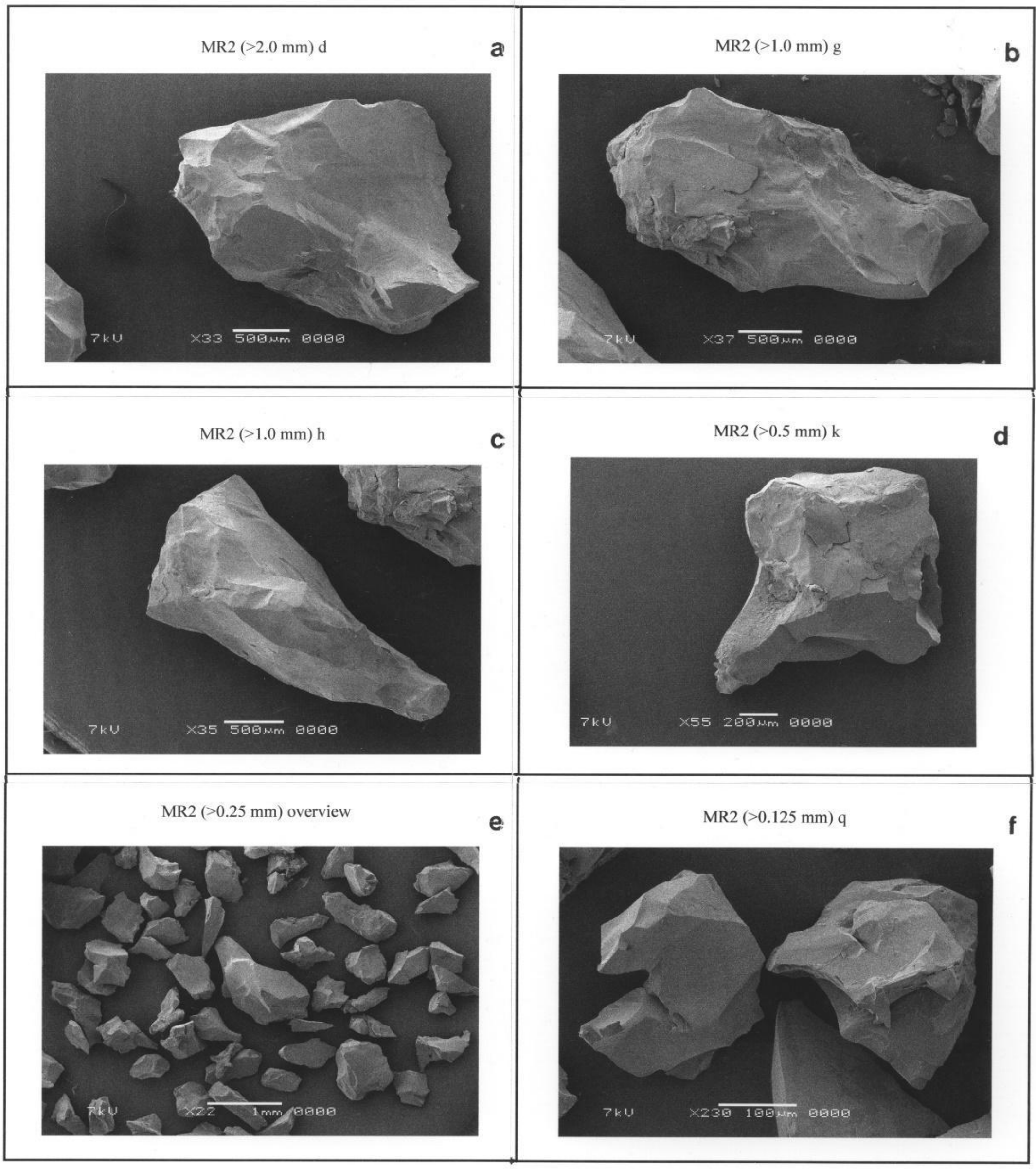
MR2 (>2.0 mm) d
a
7kV X33 500µm 0000
MR2 (>1.0 mm) g
b
7kV X37 500µm 0000
MR2 (>1.0 mm) h
c
7kV X35 500µm 0000
MR2 (>0.5 mm) k
d
7kV X55 200µm 0000
MR2 (>0.25 mm) overview
e
7kV X22 1mm 0000
MR2 (>0.125 mm) q
f
7kV X230 100µm 0000

Figure 4

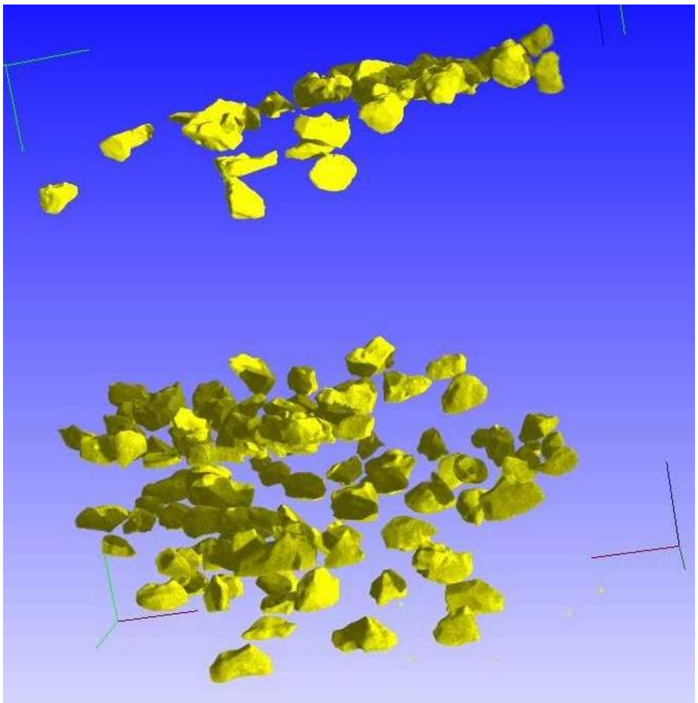

Figure 5

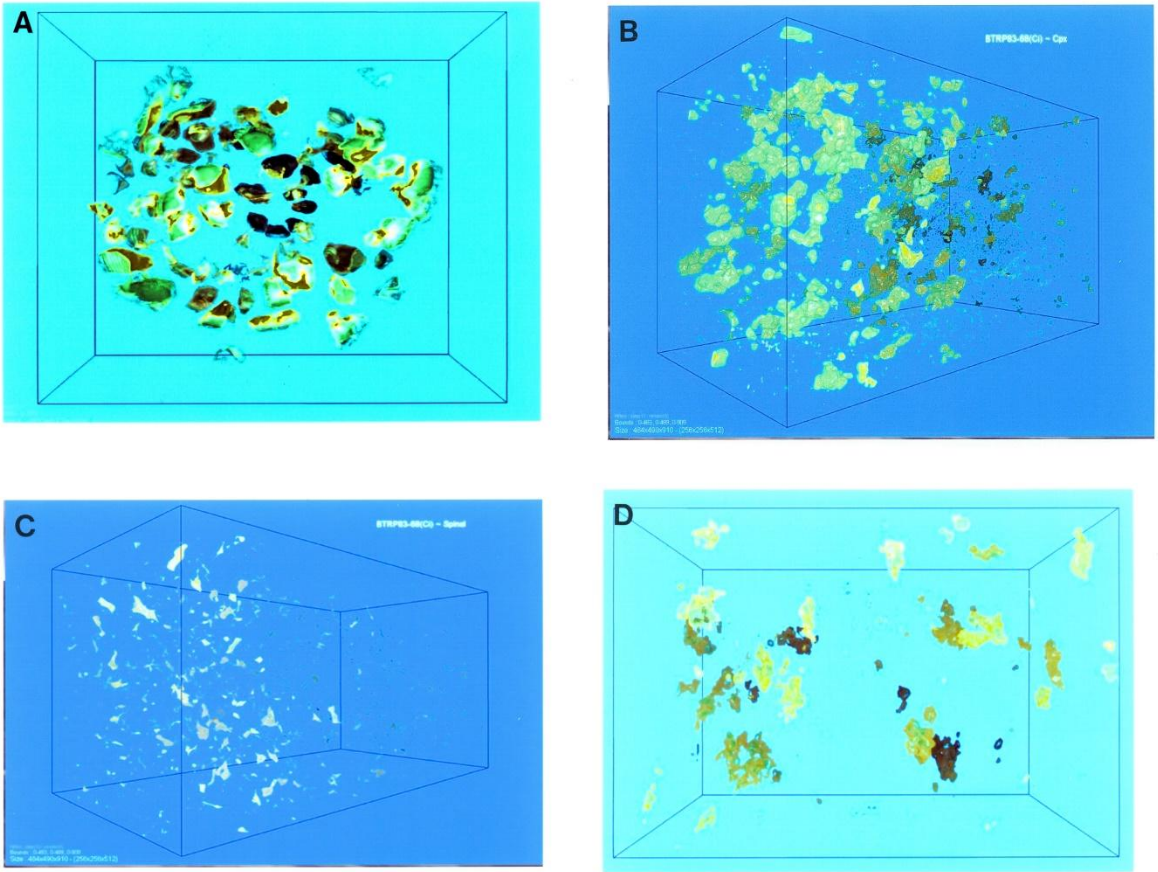

Figure 6

$P = 4L$	$P = \pi D$	$P = 6L$	$P = 3L$
$A = L^2$	$A = \pi D^2/4$	$A = (3^{3/2}L^2)/2$	$A = (\sqrt{3}/4)L^2$
$R = 4$	$R = 2\sqrt{\pi}$	$R = (\sqrt{8})3^{1/4}$	$R = 3/(\sqrt{3}/4)^{1/2}$

Figure 7

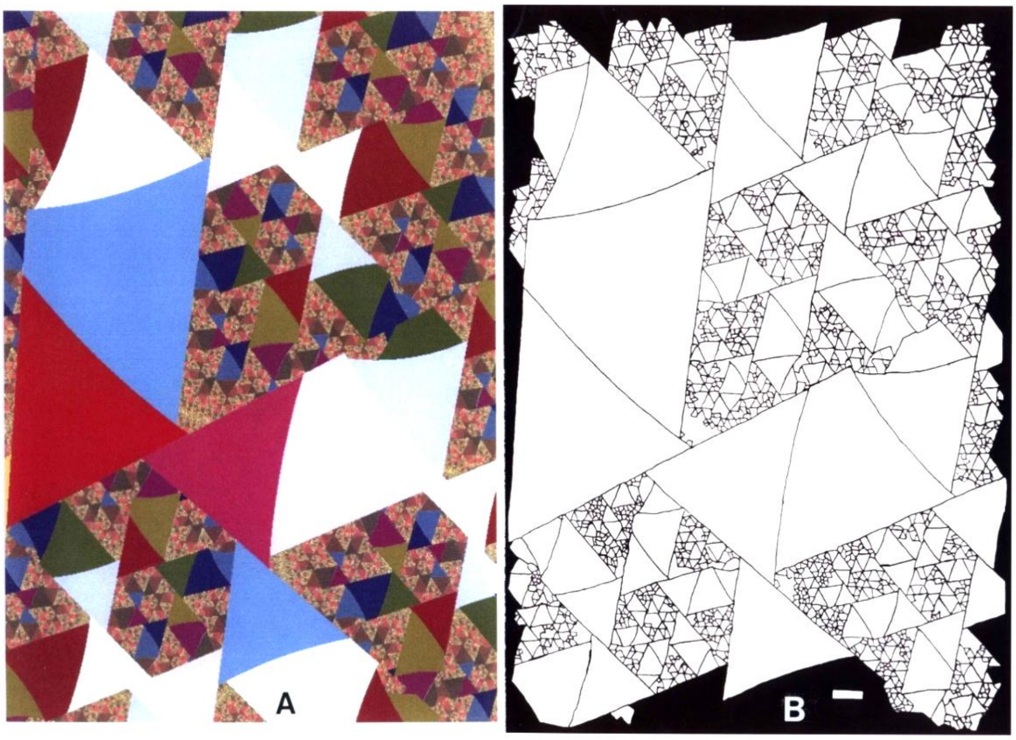

Figure 8

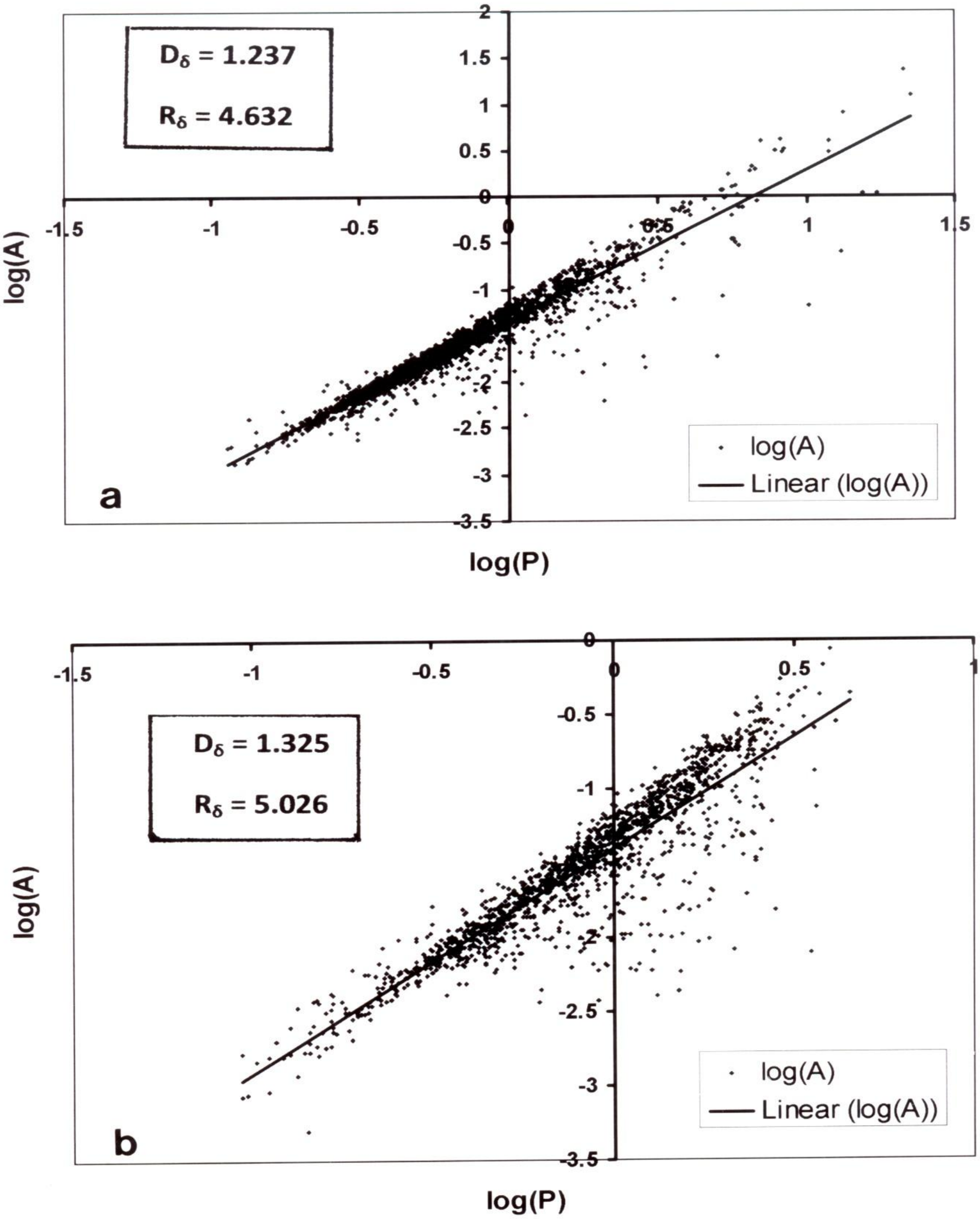
D_δ = 1.237
R_δ = 4.632
log(A)
Linear (log(A))
a
log(A)
log(P)
D_δ = 1.325
R_δ = 5.026
log(A)
Linear (log(A))
b
log(A)
log(P)

Figure 9

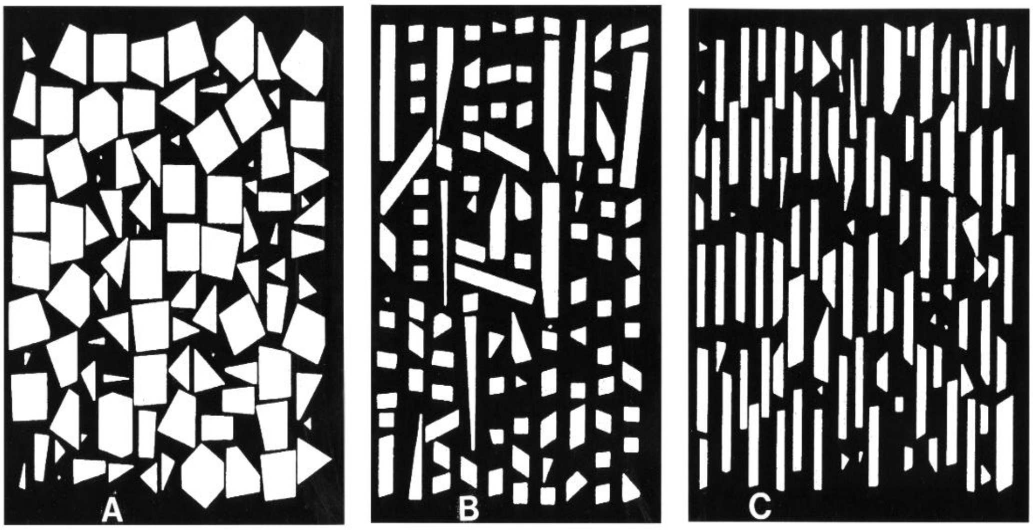

Figure 10

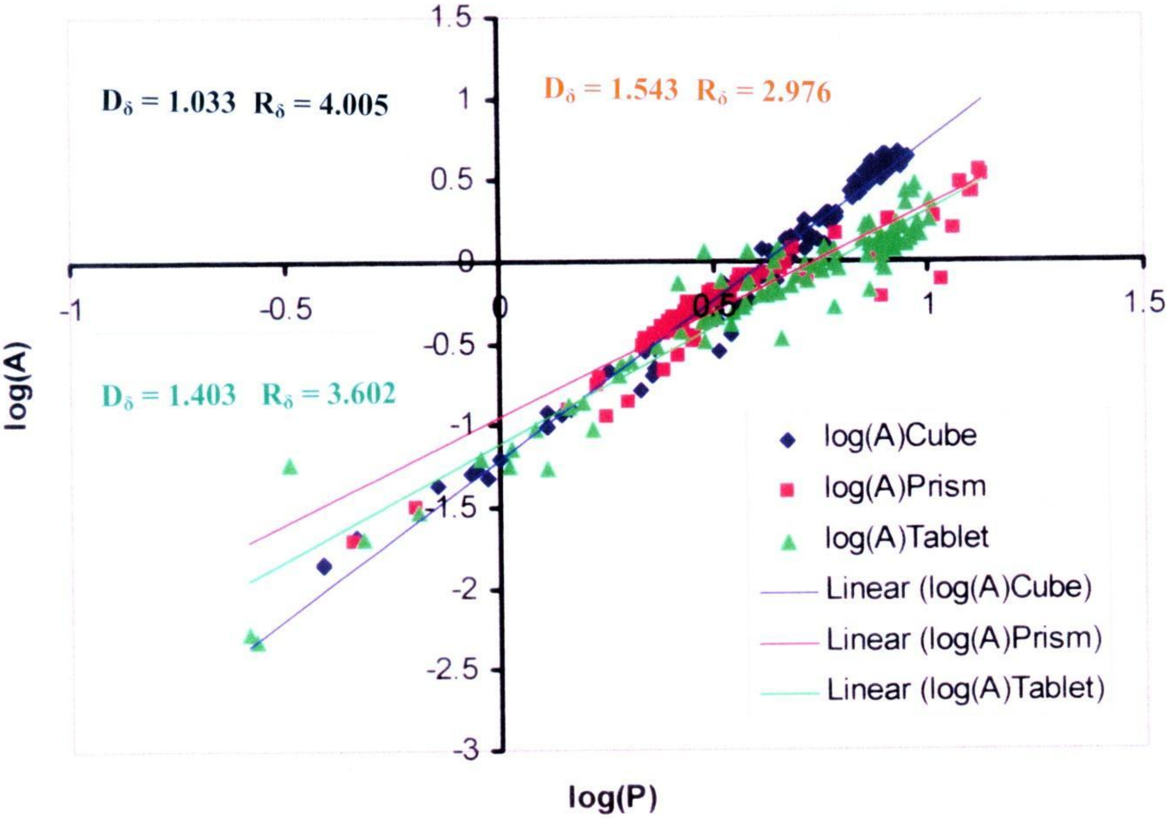

D_δ = 1.033 R_δ = 4.005
D_δ = 1.543 R_δ = 2.976
D_δ = 1.403 R_δ = 3.602
1.5
1
0.5
0
-0.5
-1
-1.5
-2
-2.5
-3
-1
-0.5
0
0.5
1
1.5
log(A)
log(P)
log(A)Cube
log(A)Prism
log(A)Tablet
Linear (log(A)Cube)
Linear (log(A)Prism)
Linear (log(A)Tablet)

Figure 11

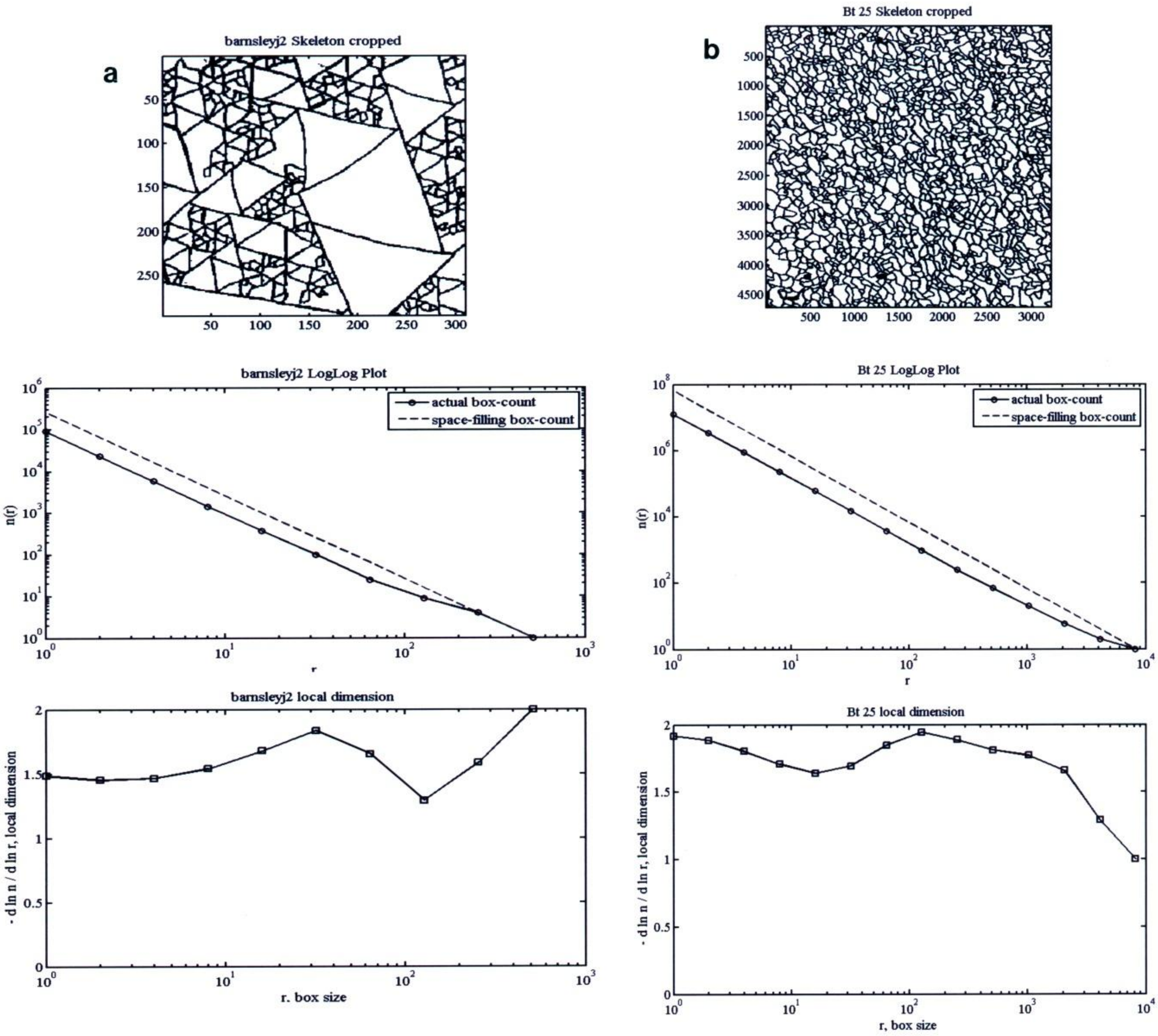
a
barnsleyj2 Skeleton cropped
b
Bt 25 Skeleton cropped
barnsleyj2 LogLog Plot
actual box-count
space-filling box-count
n(r)
r
Bt 25 LogLog Plot
actual box-count
space-filling box-count
n(r)
r
barnsleyj2 local dimension
- d ln n / d ln r, local dimension
r. box size
Bt 25 local dimension
- d ln n / d ln r, local dimension
r, box size

Table 1
Click here to download Table: TXMPRR Table 1.docx

Table 1, Results Summary, for additional spinel peridotite xenoliths from the Massif Central, France and from the volcanic district, central Spain (Calatrava).

Sample	Origin	Mean area	Standard deviation	Number of areas
RP83-68	RayPic	0.468	0.918	801
Mb-18	Montboissier	0.448	1.113	531
Mb-47	Montboissier	0.338	0.797	820
Mb-50	Montboissier	0.344	0.824	643
PH-1	Puy de la Halle	0.192	0.359	1028
PH- 2	Puy de la Halle	0.157	0.308	1347
Fr-10	Fraise	0.177	0.387	535
Fr-11	Fraise	0.268	0.648	571
ST-2	Sauterre	0.272	0.556	369
Ta-13	Tarreyres	0.325	0.649	423
Ta-39	Tarreyres	0.275	0.450	1152
MS-8	Monistrol d'Allier	0.195	0.350	1646
MS-20	Monistrol d'Allier	0.145	0.256	2054
Z-6	Zaniere	0.172	0.403	1712
Z-8	Zaniere	0.135	0.323	2259
Bt-11	Puy Beaunit	0.373	0.738	812
Bt-25	Puy Beaunit	0.102	0.120	2510
Br-9	Mont Briancon	0.330	0.609	959
Br-17	Mont Briancon	0.483	1.016	528
Bo83-73(i) ‡	Region Boree	0.399	0.830	525
Bo83-73(ii) ‡	Region Boree	0.350	0.717	880
Bo83-73(iii) ‡	Region Boree	0.320	0.626	912
Bo83-73(iv) ‡	Region Boree	0.320	0.751	748
TAB-23	Molines/Rastillas	0.297	0.621	1298
TAB-26	Molines/Rastillas	0.234	0.443	791
MR-1/(i) ‡	Molines/Rastillas	0.486	1.108	694
MR-1/(ii) ‡	Molines/Rastillas	0.471	0.964	874
MR-1/(iii) ‡	Molines/Rastillas	0.519	1.071	646
MR-2/(i) ‡	Molines/Rastillas	0.395	0.682	1016
MR-2/(ii) ‡	Molines/Rastillas	0.282	0.490	1117
MR-2/(iii) ‡	Molines/Rastillas	0.472	1.008	821
P21615(EWH1‡548)	Calatrava, Spain	0.482	0.962	641
P21616(EWH 01)	Calatrava, Spain	0.551	1.316	524
P21617(EWH 02)	Calatrava, Spain	0.655	1.873	394
P21618(EWH 03)	Calatrava, Spain	0.389	0.909	748
P21619(EWH 04)	Calatrava, Spain	0.237	0.517	748
P21620(EWH 05)	Calatrava, Spain	0.499	1.233	654
P21620(EWH 06)	Calatrava, Spain	0.469	0.852	685

‡ Sections, (i) (ii) (iii) (iv), cut from the same xenolith, at random for Bo83-73 and mutually orthogonal, (i) (ii) (iii), for MR-1 and MR-2.

Table 2
Click here to download Table: TXMPRR Table 2.docx

Table 2. Results Summary for additional Spinel peridotite xenoliths from the West German, Central European Volcanic Province (CEVP) and the Hungarian Pannonian Basin. Also from the STP Streap Com'Laidh, Scotland site.

Sample	Origin	Mean area	Standard deviation	Number of areas
GW-E G4(2)	Rudersbusch, Eifel	0.142	0.242	1770
GW-E RB1187	Rutherberg, Westerwald	0.316	0.766	886
GW-E H943	Huhnerberg, Siebengebirge	0.207	0.664	1274
GW-E BR1026	Breitenborn, Vogelsberg	0.437	0.749	754
GW-E DH1132	Dreihausen, Vogelsberg	0.558	1.209	514
DW83-20	Dreiser Weiher, Eifel	0.261	0.480	1364
DW83-20a*	Dreiser Weiher, Eifel	0.515	0.786	302
DW83-20b*	Dreiser Weiher, Eifel	0.187	0.330	787
DW83-20c*	Dreiser Weiher, Eifel	0.202	0.350	608
DW83-20d*	Dreiser Weiher, Eifel	0.192	0.338	765
D8	Deudesfeld, Eifel	0.237	0.566	1472
DE4	Deudesfeld, Eifel	0.285	0.459	1363
DQ1 Quarry	Deudesfeld, Eifel	0.213	0.307	749
DQ2 Quarry	Deudesfeld, Eifel	0.277	0.523	697
DR6 Quarry	Deudesfeld, Eifel	0.311	0.557	1108
DR8 Quarry	Deudesfeld, Eifel	0.212	0.335	1210
G95-2	Gees, Eifel	0.411	0.885	1004
SZT-1068	Szentbekalla, Hungary*	0.532	1.660	694
SZT-1068T	Szentbekalla, Hungary*	0.331	0.723	542
SZT-1068B	Szentbekalla, Hungary*	1.279	3.152	154
SZG-1006	Szigligit, Hungary	0.521	0.994	869
SZG-1043	Szigligit, Hungary	0.153	0.239	1739
G-1005	Gerce, Hungary	0.326	0.577	940
G-1007	Gerce, Hungary	0.243	0.455	2115
G-1009	Gerce, Hungary	0.209	0.386	1339
G-1009A	Gerce, Hungary	0.261	0.432	1338
G-1023(i)	Gerce, Hungary	0.261	0.414	1210
G-1023(ii)	Gerce, Hungary	0.197	0.305	1319
STC 1	Streap Com'Laidh, UK	0.208	0.387	2227
STC 3	Streap Com'Laidh, UK	0.233	0.417	1120
STC 4	Streap Com'Laidh, UK	0.169	0.290	2346
STC 9	Streap Com'Laidh, UK	0.190	0.327	2255
STC 13	Streap Com'Laidh, UK	0.082	0.129	2679
STC 14	Streap Com'Laidh, UK	0.171	0.365	1067
STC 17	Streap Com'Laidh, UK	0.215	0.422	1594
STC 18	Streap Com'Laidh, UK	0.146	0.241	2003

Table 3
Click here to download Table: TXMPRR Table 3.docx

Table 3. Results Summary for Kimberlite-hosted garnet and spinel peridotite xenoliths from Siberia and South Africa (S.A.).

Sample	Origin	Mean areas	Standard deviation	Number of areas
Y26(i) †	Udachnaya Pipe Anabar/Siberia	0.714	1.399	302
Y26(ii) †	Udachnaya Pipe Anabar/Siberia	0.829	1.530	330
Y26(Ave)	Udachnaya Pipe Anabar/Siberia	0.772	1.465	632
Y27(i) †	Udachnaya Pipe Anabar/Siberia	1.624	3.053	184
Y27(ii) †	Udachnaya Pipe Anabar/Siberia	0.952	2.019	176
Y27(Ave)	Udachnaya Pipe Anabar/Siberia	1.288	2.536	360
Y28	Udachnaya Pipe Anabar/Siberia	2.019	2.855	116
Y29	Udachnaya Pipe Anabar/Siberia	0.573	0.835	311
Y31	Udachnaya Pipe Anabar/Siberia	0.943	1.448	254
Y32	Udachnaya Pipe Anabar/Siberia	1.253	1.804	108
Y33	Udachnaya Pipe Anabar/Siberia	0.589	0.864	349
BRD1	Boshoff Road Dump Kimberly S. A.	1.876	2.515	88
BRD2	Boshoff Road Dump Kimberly S. A.	0.680	1.023	697
BRD(Ave)	Boshoff Road Dump Kimberly S. A	1.278	1.769	785
TE201(1) †	Garnet Harzburgite S. A.	0.391	2.196	460
TE201(2) †	Garnet Harzburgite S. A.	0.688	2.626	523
TE201(3) †	Garnet Harzburgite S. A.	0.390	1.864	580
TE201(4) †	Garnet Harzburgite S. A.	0.498	2.233	609
TE201(5) †	Garnet Harzburgite S. A.	0.363	1.618	691
TE201(6) †	Garnet Harzburgite S. A.	0.543	2.972	551
TE201(7) †	Garnet Harzburgite S. A.	0.491	1.732	575
TE201(8) †	Garnet Harzburgite S. A.	0.473	2.027	607
TE201(Ave)	Garnet Harzburgite S. A.	0.480	2.159	4596
TE294/DB1(1) †	Garnet Peridotite, De Beers, S. A.	2.960	5.306	122
TE294/DB1(2) †	Garnet Peridotite, De Beers, S. A.	1.961	4.299	174
TE294/DB1(3) †	Garnet Peridotite, De Beers, S. A.	3.457	6.551	118
TE294/DB1(4) †	Garnet Peridotite, De Beers, S. A.	2.359	6.049	148
TE294/DB1(5) †	Garnet Peridotite, De Beers, S. A.	1.754	3.531	201
TE294/DB1(6) †	Garnet Peridotite, De Beers, S. A.	3.718	7.199	83
TE294/DB1(7) †	Garnet Peridotite, De Beers, S. A.	3.115	6.468	112
TE294/DB1(8) †	Garnet Peridotite, De Beers, S. A.	2.634	8.495	103
TE294/DB1(Ave)	Garnet Peridotite, De Beers, S. A.	2.748	5.987	1061

† Multiple sections, cut at random, from one single xenolith.

Table 4
Click here to download Table: TXMPRR Table 4.docx

Table 4. Results Summary for spinel peridotite samples from tectonically emplaced massifs.

Sample	Origin	Mean areas	Standard deviation	Number of areas
FR1/3a‡	Fontet Rouge, Pyrenees	0.401	0.868	512
FR1/3b‡	Fontet Rouge, Pyrenees	0.421	0.868	426
FR1/5a‡	Fontet Rouge, Pyrenees	0.392	0.797	491
FR1/5b‡	Fontet Rouge, Pyrenees	0.423	0.907	449
FR1/7a‡	Fontet Rouge, Pyrenees	0.317	0.616	480
FR1/7b‡	Fontet Rouge, Pyrenees	0.388	0.820	403
TE 367A	Lherz Massif, Southern France	0.354	0.621	1940
TE 362	Ronda, Southern Spain	0.172	0.537	1589
Ig - 22	Harzburgite, Goro, Indonesia	0.166	0.419	1249
TE 39/1†	Dunite, Mt. Dun, New Zealand	0.171	0.383	248
TE 39/2†	Dunite, Mt..Dun, New Zealand	0.210	0.513	275
TE 39/3†	Dunite, Mt. Dun, New Zealand	0.205	0.447	281
TE 39/4†	Dunite, Mt. Dun, New Zealand	0.227	0.422	260

†Multiple sections, cut at random, from one single sample.
‡Multiple sections, cut at random, from one single sample but measured in two approximately equal halves, a and b.

Table 5
Click here to download Table: TXMPRR Table 5.docx

Table 5. Measured Dimensions (**D_δ**) and Shape Factors (**R_δ**) from log (A) vs log (P) plots.

Shape Designation	Measured Dimension	Measured Shape Factor
Barnsleyj2 Fig. 8a	1.237	4.632
Xenolith RP91-7 Fig. 8b	1.325	5.026
Range for all samples examined	1.12 – 1.40	4.2 – 5.2
Combined sections A+B+C Fig. 9	1.268	3.525
Cube sections Fig.10	1.033	4.005
Prism sections Fig. 10	1.543	2.976
Tablet sections Fig. 10	1.403	3.602